Magnetic Hammer Actuation for Tissue Penetration using Millirobots

Julien Leclerc, Ashwin Ramakrishnan, Nikolaos V. Tsekos, and Aaron T. Becker

Abstract— Untethered magnetic navigation of millirobots within a human body using an MRI scanner is a promising technology for minimally invasive surgery or drug delivery. Because MRI scanners have a large static magnetic field, they cannot generate torque on magnetic millirobots and must instead use gradient-based pulling. However, gradient values are too small to produce forces large enough to penetrate tissue. This paper presents a method to produce large pulsed forces on millirobots. A ferromagnetic sphere is placed inside a hollow robot body and can move back and forth. This movement is created by alternating the magnetic gradient direction. On the posterior side, a spring allows the sphere to change direction smoothly. On the anterior side, a hard rod creates a surface for the sphere to impact. This impact results in a large pulsed force. This paper begins with modeling and simulating this system. Next, a control strategy is presented and experimentally tested. Finally, preliminary tests inside a clinical MRI scanner demonstrate the potential of this actuation system.

I. INTRODUCTION

The navigation of millimeter-scale robots through the passageways of bodies is currently being studied as a method to perform highly localized drug delivery or perform minimally invasive surgery [1]–[3]. Untethered navigation can be achieved by placing a ferromagnetic piece inside the robot and producing a controlled magnetic field around a patient. Propulsion and steering of millirobots can be accomplished by either moving a permanent magnet assembly around a patient [4] or by controlling the current inside electromagnets [5]. The latest solution is often realized with an MRI scanner which already includes several electromagnets. In an MRI, the background field magnetizes the ferrous components of the robot, and the gradient coils generate the magnetic gradient necessary to produce forces. The MRI scanner can be used simultaneously to provide real-time imaging of the operating area as well as positioning of the robot.

The force generated on the millirobots is proportional to the field gradient strength. Commercial MRI scanners produce gradients in the range of 20 to 40 mT/m. These gradients are sufficient to maneuver milli-robots inside fluid-filled regions of the body, such as vessels, [6] but insufficient for tissue penetration that requires larger forces [7]; tissue penetration is required for many procedures, including brachytherapy and micro-biopsy. This paper presents a method, denoted *magnetic hammer actuation*, that can generate large pulsed forces for tissue penetration. The magnetic hammer is a system embedded into the millirobot.
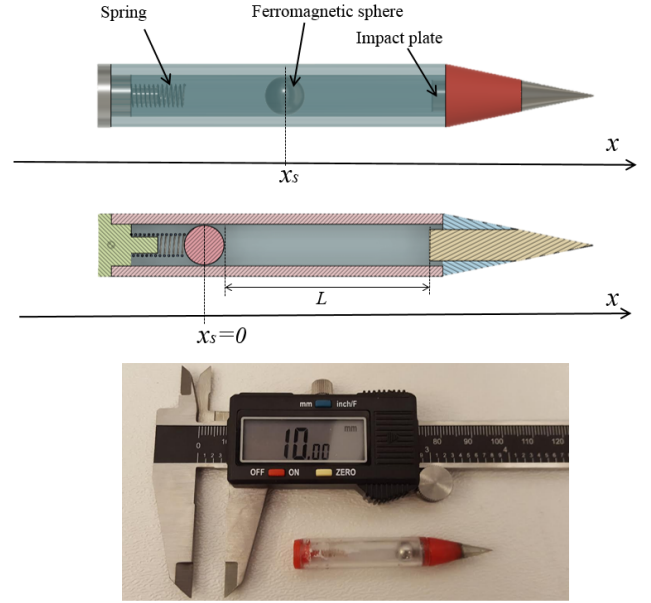
Fig. 1. Schematic representation of a millirobot actuated by a magnetic hammer (top), hardware prototype (bottom).

The millirobot has a tubular structure in which a ferromagnetic sphere can move back and forth. This movement is produced by alternately changing the gradient direction. On the posterior side of the millirobot, a spring allows the sphere to change direction smoothly. On the anterior side, a hard rod creates a surface for the sphere to impact, the *impact plate*. This impact results in large pulsed forces that enable penetrating body tissues progressively. A magnetic test bench has been developed to make experimental tests more practical and less expensive. It includes coils, sensors, power electronics, and a real-time controller.

The paper is organized as follows: first, the system is mathematically modeled, and its behavior is studied in section II. Secondly, parameters for the model are experimentally measured (see section III). Different materials for the impact plate are compared. Thirdly, the magnetic test bench is described and the test of a magnetic hammer is presented (see section IV). Results are compared to the mathematical model. Next, preliminary results from an open-loop test performed in a clinical MRI scanner are presented in section V. The last section (section VI) is a conclusion of this study.

II. THEORETICAL STUDY

A. Mechanical modelization

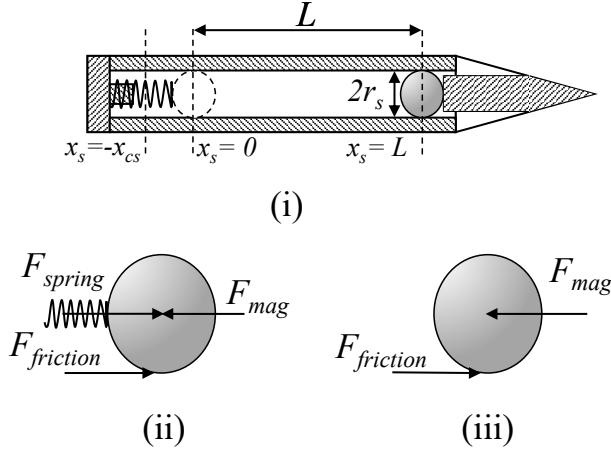The motion of the sphere between two consecutive impacts can be divided into two phases, based on the forces that

Fig. 2. (i) Free length of sphere travel, L; (ii) Free body diagram of sphere when spring is compressed, (iii) when spring is not compressed

Fig. 3. Closed loop impact velocity for 150 impacts; k = 50 N/m; e = 0.9; F_{mag} = 1.5e-3 N; L = 0.03 m; m_s = 5.58e-4 kg; r_s = 2.5 mm.

act on it. The magnetic gradient force F_{mag} and friction force $F_{friction}$ act on the sphere during its motion along the free length of the tube, L (See Fig. 2 (i),(iii)). When the spring is compressed, its reaction force F_{spring} acts on the ball as well (See Fig. 2 (ii)). The directions of F_{mag} and $F_{friction}$ change depending on the direction of motion of the sphere. Inside the homogeneous region of an MRI scanner, the magnitude of F_{mag} is constant [8]. The same has been assumed for developing analytical and numerical models in this paper. The formula for calculating F_{mag} is presented in section II-B. Friction is considered to be negligible, but the assumption will be relaxed in later sections. The spring force is straightforward, and is given by

$$F_{\text{spring}} = kx, \tag{1}$$

where x is the compression length, and k is the spring constant. To maximize the average impact velocity over an arbitrary n number of contacts, the input magnetic gradient should always be in the same direction as the motion of the sphere. This is equivalent to a perfectly closed-loop system where the gradient signal switches direction when the sphere switches direction.

An analytical model was developed by solving the system ODE to predict the impact velocity for each impact, given a set of input parameters. The sphere-impact plate system is assumed to have a coefficient of restitution, e. This model assumes that the robot capsule does not move. The impact velocities for different values of e are plotted in fig. 3. For all values of e, the impact velocity initially increases and ultimately saturates, reaching a resonant value. This happens when the energy lost by the sphere during impact equals the energy gained by it during the rest of the cycle. As expected, a higher e results in a higher impact velocity. Figure 5 shows a sample closed-loop pulsed magnetic gradient input for 50 impacts. The frequency initially varies until it settles to a constant value at resonance. An analytical formula was derived to predict the resonant impact velocity, for a given
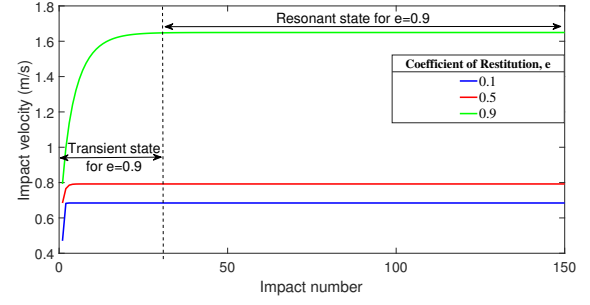
set of input parameters. This is given by eq. (2).

$$v_{\text{res}} = \frac{2\sqrt{\frac{F_{\text{mag}}\left((e^2+1)F_{\text{mag}}+(e^2-1)(-k)L+\sqrt{(2-2e^4)kLF_{\text{mag}}+(1+e^2)^2 F_{\text{mag}}^2}\right)}{km_s}}}{1-e^2} \tag{2}$$

In the above equation, m_s is the mass of the sphere in kgs. The radius of the ball r_s indirectly influences the impact velocity through F_{mag} and m_s, both of which depend on the volume of the sphere. The variation of v_{res} with changes in $L, e, k, m_s, r_s, F_{mag}$ were plotted and they were all found to be monotonic functions with no critical points. Further, the time between impacts at resonance t_{res}, is a constant value and is given by eq. (3).

$$t_{res} = t_{pos,1} + t_{pos,2} + t_{ant,1} + t_{ant,2} \tag{3}$$

$$t_{pos,1} = \frac{\sqrt{e^2 v_{\text{res}}^2 + \frac{2LF_{\text{mag}}}{m_s}} - ev_{\text{res}}}{\frac{F_{\text{mag}}}{m_s}} \tag{4}$$

$$t_{pos,2} = \frac{\pi - \tan^{-1}\left(\frac{k\sqrt{e^2 v_{\text{res}}^2 + \frac{2LF_{\text{mag}}}{m_s}}}{\omega F_{\text{mag}}}\right)}{\omega}; \omega = \sqrt{\frac{k}{m_s}} \tag{5}$$

$$t_{ant,1} = \frac{\cos^{-1}\left(\frac{F_{\text{mag}}}{F_{\text{mag}}+kx_{cs}}\right)}{\omega} \tag{6}$$

$$t_{ant,2} = \frac{v_{\text{res}} - \sqrt{v_{\text{res}}^2 - \frac{2LF_{\text{mag}}}{m_s}}}{\frac{F_{\text{mag}}}{m_s}} \tag{7}$$

$$x_{cs} = \frac{\sqrt{e^2 km_s v_{\text{res}}^2 + 2kLF_{\text{mag}} + F_{\text{mag}}^2} + F_{\text{mag}}}{k} \tag{8}$$

In the above equations, x_{cs} is the maximum compression distance of the spring (See Fig. 2 (i)), and ω represents the natural frequency of the spring-mass system. The value of x_{cs} can be used to select an appropriate free length for the spring, to ensure that it does not bottom out during compression. The values $t_{pos,1}$, $t_{pos,2}$, $t_{ant,1}$ and $t_{ant,2}$ represent the time for the ball to move from x_S = (i) L to 0, (ii) 0 to $-x_{cs}$, (iii) $-x_{cs}$ to 0, and (iv) 0 to L respectively, in a perfectly closed-loop system with optimal gradient switching.
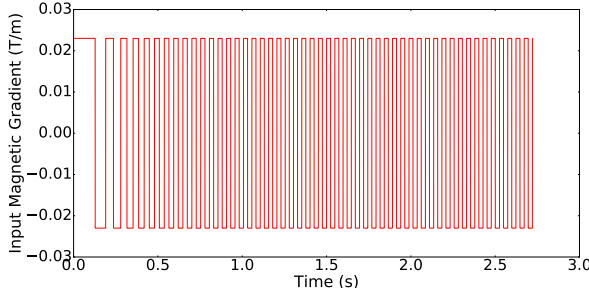
¡¡¡¡¡¡¡ HEAD

Fig. 4. Closed loop input gradient for 50 impacts; k = 50 N/m; e = 0.9; F_{mag} = 1.5e-3 N; L = 0.03 m; m_s = 5.58e-4 kg; r_s = 0.0025 m.

Fig. 5. Closed loop input gradient for 50 impacts; k = 50 N/m; e = 0.9; F_{mag} = 1.5e-3 N; L = 0.03 m; m_s = 5.58e-4 kg; r_s = 0.0025 m.
¿¿¿¿¿¿¿ origin/master

B. Magnetic field calculation

The magnetic field generated by an MRI scanner can be separated into two components. The first is a constant and strong magnetic field B_0 along the z-axis. This field is used to align the magnetic moments of the protons. Commercial MRI scanners have B_0 typically ranging from 1.5 to 3 T. The second component of the field is the magnetic gradient. It is used to encode the MRI signal spatially. The flux density $\mathbf{G}$ produced by the gradient coils is added to $\mathbf{B_0}$ and linearly varies with position. A computer controls this value.

The modelization of the field inside the uniformity sphere of an MRI scanner is straightforward. $\mathbf{G}$ is directly proportional to the current inside the gradient coils.

$$\mathbf{B} = \mathbf{B_0} + \mathbf{G}, \quad \mathbf{B_0} = \begin{bmatrix} 0 \\ 0 \\ B_0 \end{bmatrix}, \quad \mathbf{G} = \begin{bmatrix} k_x I_x \\ k_y I_y \\ k_z I_z \end{bmatrix} \quad (9)$$

where k_x, k_y and k_z are the coil constants (T/A) and I_x, I_y and I_z are the electrical current values.

The flux density is more complicated to calculate outside of the uniformity sphere. The same problem is present in our desktop experiment because the flux density and gradient are not constant. To calculate forces accurately, it is necessary to compute the magnetic field precisely. A semi analytical method was used to calculate the field produced in all space by a solenoid assembly. It was tested on our desktop experiment.

According to [9], the magnetic flux density produced by a current loop in all space can be calculated using equations eqs. (10) to (13) and fig. 6. $E(k)$ and $K(k)$ are the complete elliptical integrals of first and second kind respectively.

$$B_z = \frac{\mu_0 I}{2\pi\delta^2\beta} \left[\left(a^2 - \rho^2 - z^2\right)\left(E(k^2) + \delta^2 K(k^2)\right) \right] \quad (10)$$

$$B_\theta = \frac{\mu_0 I \cdot z}{2\pi\delta^2\beta\rho} \left[\left(a^2 - \rho^2 - z^2\right)\left(E(k^2) - \delta^2 K(k^2)\right) \right] \quad (11)$$

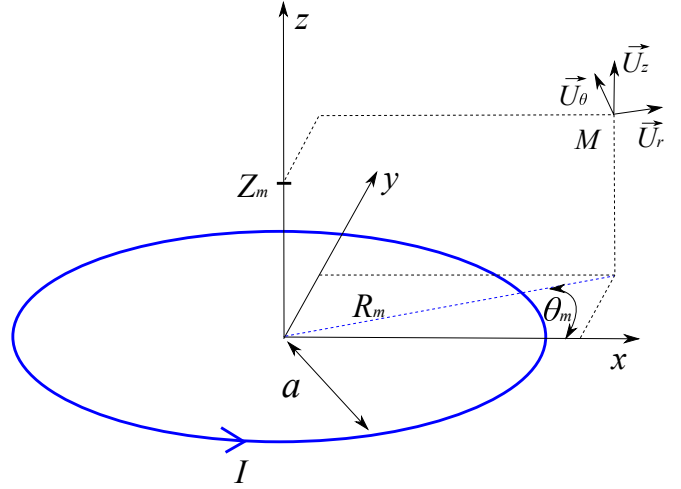$$\delta = \sqrt{a^2 + R_m^2 + Z_m^2 - 2aR_m} \quad (12)$$

Fig. 6. Geometry and variables used in equation eqs. (10) to (13)

$$\beta = \sqrt{a^2 + R_m^2 + Z_m^2 + 2aR_m} \quad (13)$$

The cross-section S of any solenoid can be divided into infinitesimal sections dS. Each dS is subjected to a current $dI = JdS$. This current dI forms an infinitesimal loop, and the field it produces can be calculated using eqs. (10) to (13). By integrating this equation over the solenoid cross-section, one can obtain the value of the flux density generated by the solenoid.

The flux density must be calculated for each solenoid. The total flux density is the vectorial sum of the flux density produced by each solenoid. The results obtained via this semi analytical method is compared to the solution obtained via finite element calculations with the software FEMM [10] (see fig. 7). The results are identical. The semi-analytical method is faster to compute for this model. Indeed, the magnetic field only needs to be calculated at the sphere position. The semi-analytical method can calculate the magnetic field at one point only whereas, finite elements methods must compute the magnetic field in the full domain.

C. Magnetic force calculation

This section calculates the force applied by the magnetic field to the sphere.

The ferromagnetic sphere is small compared to the coil system and can be considered as a infinitely small magnetic moment $\mathbf{m}$. Assuming a constant material magnetization $\mathbf{M}$, one can calculate $\mathbf{m}$ from eq. (14).

V is the volume of the sphere. The ferromagnetic sphere is magnetized by the externally applied field $\mathbf{H}_{app} = \mathbf{B}_{app}/\mu_0$. Ferromagnetic materials create a demagnetizing field $\mathbf{H}_d$ when subjected to an external field. The actual field $\mathbf{H}$ seen by the sphere is the sum of $\mathbf{H}_{app}$ and $\mathbf{H}_d$. This effect must be taken into account to calculate the magnetization accurately. $\mathbf{H}_d$ is related to $\mathbf{H}_{app}$ by eq. (15). The demagnetization factor N for a sphere is -1/3. Its magnetization can be calculated using eq. (16). Once the magnetic moment $\mathbf{m}$ is obtained, the force on the sphere can be calculated using eq. (17).
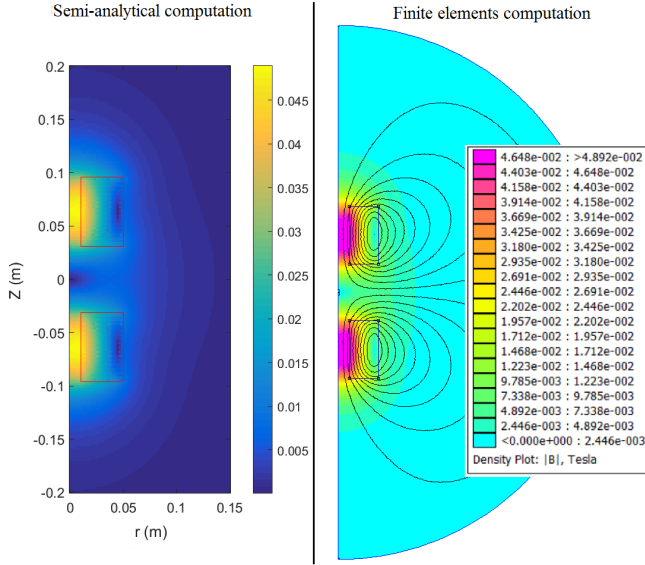
Fig. 7. Comparison between the flux density computed with the semi-analytical method with MATLAB and the flux density computed via a finite element method with FEMM.
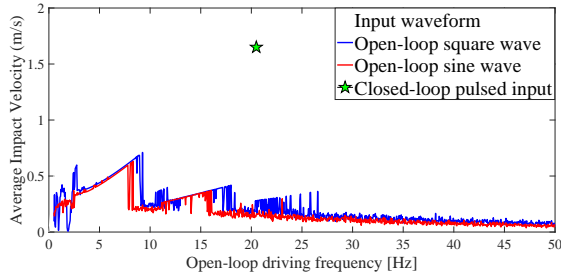

Fig. 8. Comparison of average impact velocities between closed-loop and open-loop inputs. The average was calculated over impacts 100 to 200 for the open-loop inputs.

$$\mathbf{m} = \mathbf{M}.V \tag{14}$$

$$\mathbf{H}_d = N.\mathbf{H}_{app} \tag{15}$$

$$\mathbf{M} = \frac{\mathbf{H}_{app}\left(\mu_r - 1\right)}{2.N.\mu_r - 1} \tag{16}$$

$$\mathbf{F} = \nabla(\mathbf{m}.\mathbf{B}) \tag{17}$$

D. Simulation results

1) Perfectly closed loop vs. open loop system: A numerical model was used to simulate the system dynamics for different input gradients. Average impact velocities over impacts 100 to 200 were compared for a perfectly closed loop pulsed input, and open loop inputs with sinusoidal and square profiles. As seen in figure 8, closed loop control produces approximately three times greater average impact velocity as compared to open loop sinusoidal and square waves, over all frequencies. As with the analytical model in section II-A, the simulation assumes that the robot capsule does not translate along its axis. While the absolute values of impact velocity and force will be different when the capsule is free to
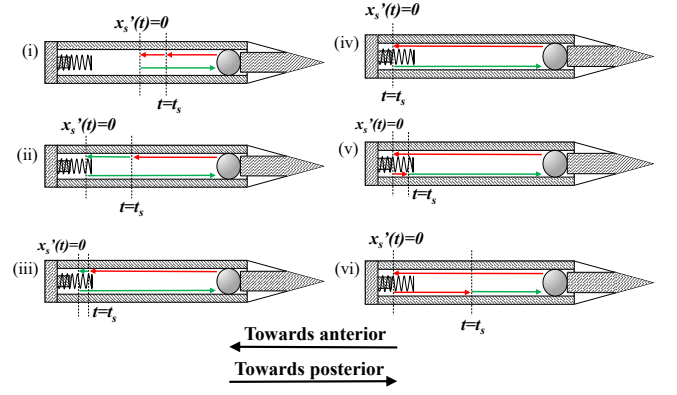

Fig. 9. Six domains for spring-end switching time; red and green represent F_{mag} towards anterior and posterior respectively. Direction of colored arrow represents direction of ball motion.

move, the closed-loop input can still be expected to produce higher forces than open-loop inputs. Further, for a given open-loop frequency, the variation of impact velocity over multiple contacts was found to be random for both square and sinusoidal inputs. It is not possible to reach the resonant state using a constant frequency input of any form. For a given set of input parameters, there exists only one path, or control input, that enables the system to reach a resonant state.

2) Partially closed loop system: To implement a perfectly closed loop system, sensing is required at both the spring and impact ends. While sensing at the impact end can be done using a microphone sensor (see section III-B), it is harder to detect sphere reversal at the spring end. For experiments of the magnetic hammer on our test bench, a partially closed-loop system was implemented with only impact end sensing using a microphone. The sensor detected each impact and triggered a reversal in the direction of the gradient force. The switching time t_s at the spring end was manually set at different values. There are six regimes for t_s, for a given set of geometric and material properties as shown in fig. 9. In fig. 9(i), the initial velocity v_{0+} and t_s are low enough that the sphere reverses direction before reaching the spring. In this case, $v_{0+} < 2aL$, where $a = F_{mag}/m_s$. Fig. 9(ii) represents the case when v_{0+} is high enough that spring compression is unavoidable even for $t_s = 0$. In fig. 9(iii), the signal switch happens after spring compression starts but before it bottoms out. Fig. 9(iv) represents perfect closed loop switching. In fig. 9(v), the signal is switched after maximum compression, but before the sphere reaches $x_s = 0$. Fig. 9(vi) represents switching after spring rebound and before the next impact. There is also a possible seventh case where the switching happens after one entire impact cycle. This case is not relevant and serves more as an upper limit of practical t_s values.

Simulations were done for the partially closed loop system to identify effects of different t_s values. The variation of time between impacts Δt_{imp}, with changes in t_s and initial velocity v_{0+} have been plotted. In fig. 10, it is seen that
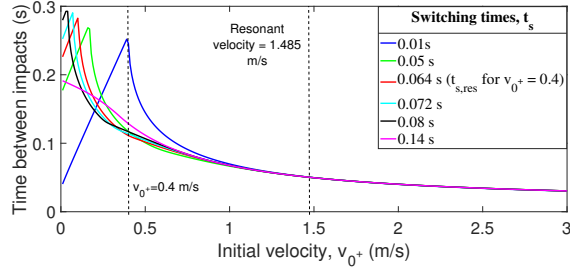
Fig. 10. Time between impacts vs. initial velocity v_{0+}, for different spring-end switching times t_s.

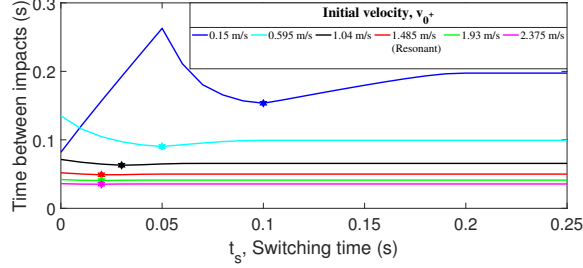
Fig. 11. Time between impacts vs. switching times t_s, for different initial velocities v_{0+}.

Δt_{imp} increases linearly, then starts dropping. For a given t_s, the linearly increasing region represents the case where the ball reverses before reaching the spring (See fig. 9(i)). Beyond the critical point, the sphere compresses the spring and reaches the impact plate faster for higher values of v_{0+}. For higher values of t_s, the linear region disappears for low v_{0+} values because the sphere is not brought to rest before reaching the spring. For high values of v_{0+}, Δt_{imp} converges for all values of t_s because the switching happens after the sphere completes an impact cycle. Further, it is seen that for a given value of v_{0+}, the time between impacts is lowest for the resonant value of t_s calculated from eq. (3).

Fig. 11 shows Δt_{imp} as a function of t_s. For $v_{0+} = 0.15$ m/s, there is a linear increase in Δt_{imp} till t_s reaches a critical point. This linear region represents the case shown in fig. 9(i). Beyond this, Δt_{imp} decreases with increasing t_s (fig. 9(ii),(iii)), until the latter reaches its perfectly closed-loop value. At this point Δt_{imp} reaches a minimum value (fig. 9(iv)). As t_s increases beyond this, the Δt_{imp} keeps increasing (fig. 9(v),(vi)), until it saturates because the signal is switched after the duration of the entire impact cycle. The linear range does not exist for higher values of v_{0+}. Using these models, we intend to design a control law that will help push t_s values closer to perfectly closed-loop values for subsequent impacts.

III. EXPERIMENTAL DETERMINATION OF IMPACT COEFFICIENT OF RESITITUTION

The coefficient of restitution e was determined using the time interval between two consecutive bounces of the sphere when dropped from a given height onto the impact rod. The
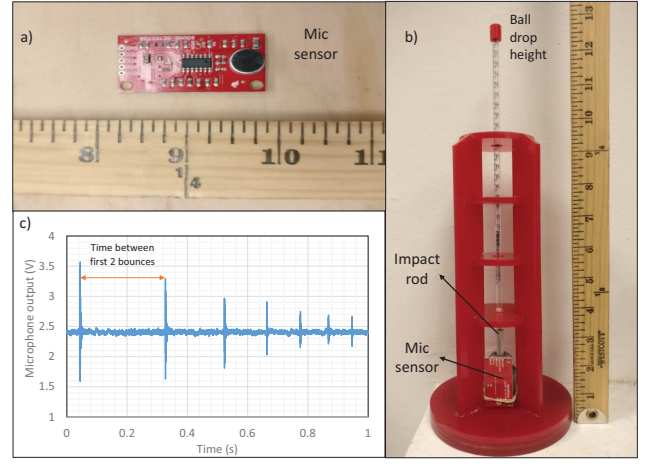

Fig. 12. Experimental setup for measuring the coefficient of restitution e
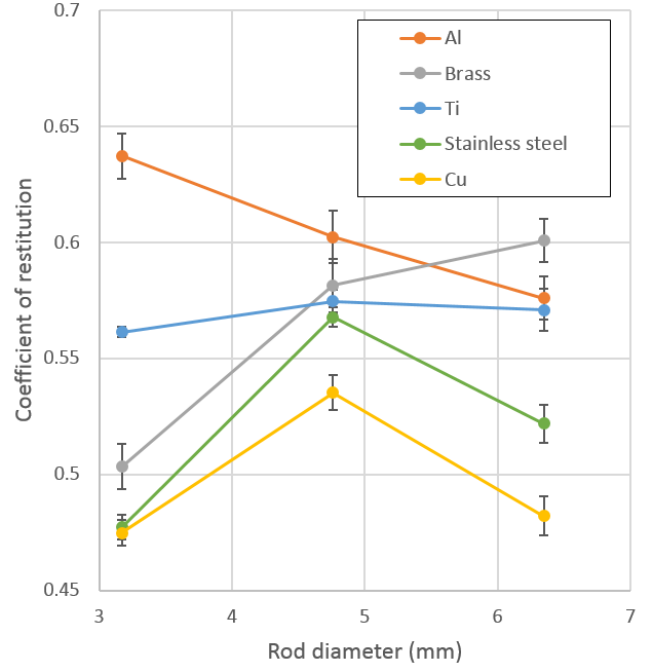

Fig. 13. Measured coefficient of restitution e as a function of rod diameter for different materials

measurements were made using 38.1 mm long impact rods for five different materials. Impact rods were held by a drill chuck. A length of 10.0 mm of the impact rods was sticking out of the chuck. The experimental setup is shown in fig. 12.

The results, shown in fig. 13, show that and that aluminum offers the largest coefficient of restitution, followed by titanium and brass. The densities of aluminum, titanium, stainless steel, brass, and copper are 2720, 4500, 7600, 8500, and 8940 kg/m^3 respectively. This data, coupled with a desire for a lightweight millirobot suggests that aluminum is the best material for an impact plate. Bio-compatibility of the material used is another constraint.
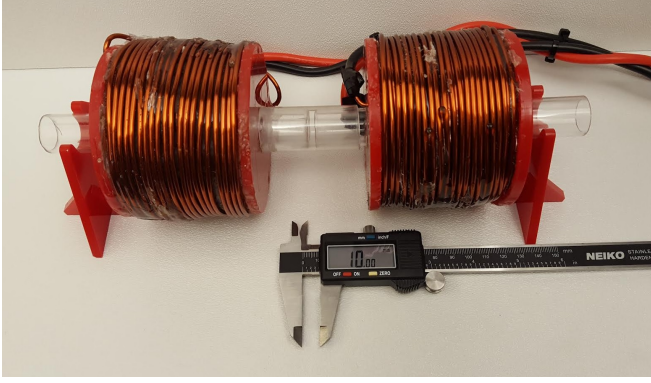
Fig. 14. Picture of the desktop-size magnetic setup.

TABLE I
PROPERTIES OF THE COILS USED IN THE DESKTOP-SIZE TEST BENCH

Internal Radius	12.7 mm	Electrical resistance	0.16 Ω
External Radius	45.8 mm	Inductance	1.59 mH
Length	65 mm	Max current change rate Voltage = 25 V	15.7 kA/s
Wire	10 AWG	Max continuous current	15 A
Wire cross-section	5.26 mm^2	Flux density on system center I = 15 A, d = 50 mm	11 mT
Number of turns	265	Gradient on system center I = 15 A, d = 50 mm	0.45 T/m

IV. EXPERIMENTAL MAGNETIC HAMMER TESTS

A. Magnetic test bench description

A desktop-size, single-axis magnetic setup was built to reduce the cost related to clinical MRI experiments. It is composed of two solenoid coils oriented along the same axis and separated by a distance d. The coils are used to produce both the magnetizing field and the gradient. The properties of the coils are shown in Table I.

The system is shown in fig. 14. The two coils are held by an acrylic tube. They can slide along this tube and be locked in place to adjust the distance between the two coils and therefore change the maximum field and gradient values. The acrylic tube is transparent, allowing for visual access to the robot. Each coil is powered via a Syren 25 switch mode power supply. A Hall-effect-based current sensor is used to perform a PID regulation of the current. It is necessary to control the current inside the coils and not only the voltage. Indeed, the produced magnetic field is directly proportional to the current whereas the voltage is related to the magnetic flux variation and the voltage drop produced by Joule effect losses.

Robots are inserted inside the acrylic tube holding the coils. They are held by a second, smaller tube that guides them along the system axis. Robots can be free to move along the coil axis or held in place. A picture of the system is provided in fig. 14.

B. Partially closed loop experiment

The coils are driven by square shaped current waveform. The current in the coils can either be I_{max} or 0 A. The coil will be said to be "on" when $I = I_{max}$ and "off" when $I = 0$ A.

As explained in section II-D.1, the magnetic hammer cannot work properly if the magnetic field is not synchronized with the position of the sphere. An open-loop control is inefficient, as shown in Fig. 8. The force applied on the sphere (and therefore the magnetic gradient) must change direction when the sphere hits the impact plate and when the sphere changes direction on the spring side to provide maximum impulse.

Our eventual goal is to use these robots in an MRI scanner, where MRI gradients must be shared for propulsion and position feedback [11]. The nature of our system enables simpler sensing requirements that can be accomplished with a simple microphone. The microphone is used to monitor the noise produced by the system. The impact noise creates a larger pulsed signal on the microphone output and can, therefore, be easily detected. When the impact is detected, the anterior coil is turned off while the posterior coil is turned on. The force applied on the sphere now pushes it backward, toward the spring side.

The current stays constant during a time T_s after the impact is detected. The anterior coil is subsequently turned on, and the posterior coil is turned off. The force then pushes the sphere forward. The current in the coils is changed again when another impact is detected. This process is repeated indefinitely.

T_s is manually tuned while the system is working. It is set to the value that gives the maximum oscillating frequency. This value corresponds to a gradient that changes direction when the sphere velocity is zero on the spring side. It should give the same results as the perfectly closed-loop simulations.

The partially closed-loop experiment was performed and compared to the model. Section IV shows a comparison of the optimum oscillating frequency as a function of I_{max}. The simulations are performed for a perfectly-closed loop system. When I_{max} increases, the oscillating frequency increases. The force on the sphere increases with I_{max} and consequently increases the moving speed of the sphere. This figure also shows that the model without friction has the same slope as the experimental data. However, the simulation signals are approximately 1 Hz faster than the experiment. This difference probably comes from the lack of friction in the model. The next subsection adds the effect of friction to the model.

C. Effect of friction

To improve the model accuracy, the friction between the moving sphere and the other components of the millirobot was included into the model. The sphere can be rolling or sliding inside the tube. The modelization is based on the method described in [12].

The rotation speed $\dot{\theta}$ is first computed and drag is calculated from this result.
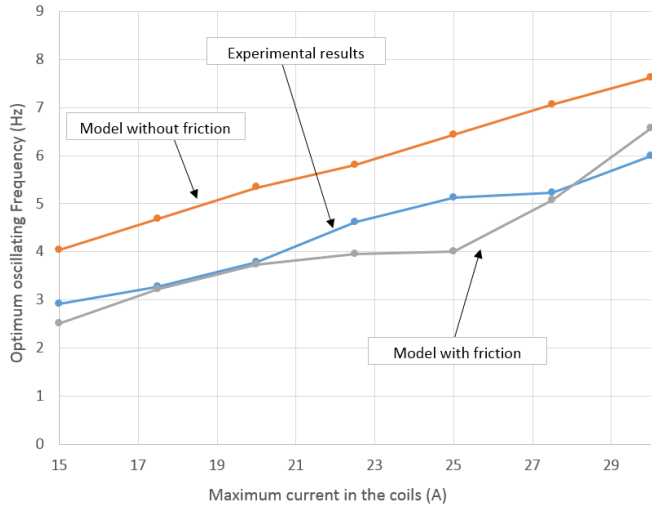
Fig. 15. Comparison between the oscillating frequency obtained experimentally and with the model as a function of the current in the coils I_{max}.

The friction on the tube produces a torque on the sphere. It is assumed that the coefficient of static friction is equal to the coefficient of kinetic friction μ_k. The equation used to calculate the angular velocity variation $\frac{\mathrm{d}\dot\theta}{\mathrm{d}t}$ of the sphere is different whether the sphere is rolling or sliding. The distinction between this two different behavior is made by calculating the relative velocities V_{rel} of the sphere and the tube surface (see eq. (18)).

$$V_{rel} = V - r\dot\theta \qquad (18)$$

If the relative speed is inferior to 0.005 m/s and if the force applied to the sphere is smaller than the kinetic friction, the sphere is considered to be rolling inside the tube and the drag is null. $\frac{\mathrm{d}\dot\theta}{\mathrm{d}t}$ can be calculated with:

$$\frac{\mathrm{d}\dot\theta}{\mathrm{d}t} = r\frac{\mathrm{d}V}{\mathrm{d}t} \qquad (19)$$

In all other cases, the torque applied to the sphere is equal to the kinetic friction force multiplied by the sphere radius. The drag is equal to the kinetic friction force $\mu_k = 0.2$.

Results of simulations are shown in Fig. 15. The addition of the friction greatly improves the model accuracy.

V. PRELIMINARY TESTS IN CLINICAL MRI

Preliminary tests of magnetic hammers were performed in a clinical 3T Siemens MRI scanner. No closed-loop control was implemented. The magnetic gradient oscillated at a constant frequency. As seen before, the system does not work optimally in these conditions. At low frequencies, the ferromagnetic sphere completely stops on both sides of the millirobot. All the kinetic energy is lost at these times, and the magnetic hammer, therefore, performs poorly. The aim of this tests is to prove that MRI scanners are suitable to produce the desired force on the magnetic sphere inside the millirobot and provide a pulsed force.
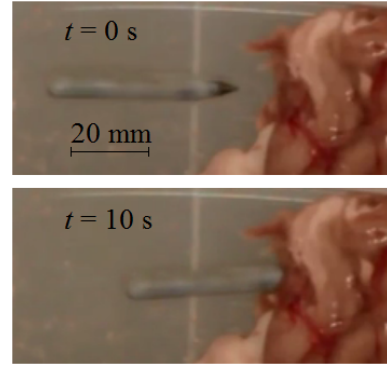

Fig. 16. Picture of the magnetic hammer driven by an MRI scanner. The penetration test is realized on a sheep brain sample.

A 50 mm long, 7 mm diameter robot was built for this test. A 2Hz square gradient with an amplitude of 23 mT/m was applied to it. This frequency is slow enough to allow the sphere to stop on both sides completely. A sheep brain hemisphere was used as tissue sample to penetrate.

Once the gradient wave was started, the sphere began to move back and forth while the robot was moving toward the sample at each impact, at an average speed of 1.9 mm/s. The robot then began to penetrate the sample. It went 9 mm deep inside it and stopped progressing (see fig. 16). This experiment demonstrated the suitability of MRI scanner to drive magnetic hammers.

Future work will implement closed loop control on the clinical MRI scanner to transfer energy efficiently. The MRI signal could be used to compute the position of the magnetic sphere at a frequency greater than 20 Hz, as we did in [11].

VI. CONCLUSIONS

A magnetic hammer system for a millirobot driven by the gradient fields of an MRI scanner was studied. The system enables producing the forces large enough to penetrate body tissue.

The hammer is composed of a ferromagnetic sphere moving inside a tube. On the posterior side of the robot, there is a spring that allows changing the direction of the sphere smoothly. On the anterior side, a hard metal rod act as an impact plate to transfer the momentum of the ferromagnetic sphere to the body of the robot.

The system is driven by an external magnetic field, such as that produced by an MRI scanner. The main field magnetizes the sphere and the gradient produces the forces necessary to move the sphere.

A complex modelization allows the computation of the position of the sphere as a function of time. The magnetic flux density and the gradient are computed using a semi-analytical method and allow an accurate calculation of the force applied to the sphere. The speed of the sphere after impact is computed from the coefficient of restitution. The rotation of the sphere is also calculated, allowing an accurate calculation of the drag produced by the sliding of the sphere inside the tube.

The coefficients of restitution e depend on the materials of the colliding objects but also on their shape and sizes. Values of e were experimentally measured. These measurements showed that aluminum impact plates have the highest values of e. This material also has the advantage of being lightweight, useful property to achieve neutral buoyancy of millirobots. In addition, titanium is a bio-compatible material. This makes titanium the best choice for impact plates of magnetic hammers.

The coefficients of restitution (e) depends on the materials of the colliding objects but also on their shape and sizes. Values of e were experimentally measured. These measurements showed that aluminum impact plates exhibit large values of e. This material also has the advantage of being lightweight, a useful property to achieve neutral buoyancy of millirobots. Titanium also performs well, is lightweight and is a bio-compatible material.

A desktop-size magnetic test bench was built to reduce experimental cost related to the use of a clinical MRI scanner. A magnetic hammer was tested with a partially closed loop control. The impact of the sphere is detected via a microphone. The posterior coil is turn on during a predetermined time to pull the sphere backward. After this time, the posterior coil is turned off and the anterior coil is turned on until the next impact is detected. Experimental results were compared to the model. The experimental oscillating frequency is in good agreement with the model predictions. This validates our modelization.

In future work, the control of the magnetic hammer will be implemented and tested in a clinical MRI scanner. The impact will be detected with the MRI signal instead of a microphone. The tradeoffs involved in miniaturization of the robot will also be studied.

REFERENCES

[1] M. Sitti, H. Ceylan, W. Hu, J. Giltinan, M. Turan, S. Yim, and E. Diller. Biomedical applications of untethered mobile milli/microrobots. *Proceedings of the IEEE*, 103(2):205–224, Feb 2015.

[2] Ajay Vikram Singh and Metin Sitti. Targeted drug delivery and imaging using mobile milli - microrobots: A promising future towards theranostic pharmaceutical design. *Current pharmaceutical design*, 22(11):1418–1428, 2016.

[3] Samara Firebaugh, Jenelle Piepmeier, Elizabeth Leckie, and John Burkhardt. Jitterbot: A mobile millirobot using vibration actuation. *Micromachines*, 2(2):295–305, 2011.

[4] Russell H Taylor. *Computer-integrated surgery: technology and clinical applications*. Mit Press, 1996.

[5] Arnaud Chanu, Ouajdi Felfoul, Gilles Beaudoin, and Sylvain Martel. Adapting the clinical mri software environment for real-time navigation of an endovascular untethered ferromagnetic bead for future endovascular interventions. *Magnetic Resonance in Medicine*, 59(6):1287–1297, 2008.

[6] Sylvain Martel, Jean-Baptiste Mathieu, Ouajdi Felfoul, Arnaud Chanu, Eric Aboussouan, Samer Tamaz, Pierre Pouponneau, LHocine Yahia, Gilles Beaudoin, Gilles Soulez, et al. Automatic navigation of an untethered device in the artery of a living animal using a conventional clinical magnetic resonance imaging system. *Applied physics letters*, 90(11):114105, 2007.

[7] A. T. Becker, O. Felfoul, and P. E. Dupont. Toward tissue penetration by mri-powered millirobots using a self-assembled gauss gun. In *2015 IEEE International Conference on Robotics and Automation (ICRA)*, pages 1184–1189, May 2015.

[8] S.S. Hidalgo-Tobon. Theory of gradient coil design methods for magnetic resonance imaging. *Concepts in Magnetic Resonance Part A*, 36A(4):223–242, 2010.

[9] James C Simpson, John E Lane, Christopher D Immer, and Robert C Youngquist. Simple analytic expressions for the magnetic field of a circular current loop. *NASA Technical report*, 2001.

[10] Finite Element Method Magnetics. http://www.femm.info.

[11] Ouajdi Felfoul, Aaron T Becker, Georgios Fagogenis, and Pierre E Dupont. Simultaneous steering and imaging of magnetic particles using mri toward delivery of therapeutics. *Scientific Reports*, 6, 2016.

[12] J Hierrezuelo and C Carnero. Sliding and rolling: the physics of a rolling ball. *Physics Education*, 30(3):177, 1995.